Transport properties of the clathrate BaGe5

Christophe Candolfi, Umut Aydemir, Alim Ormeci, Wilder Carrillo-Cabrera, Ulrich Burkhardt, Michael Baitinger, Niels Oeschler, Franck Steglich, Yuri Grin

Transport properties of the clathrate BaGe5

C. Candolfi, U. Aydemir, A. Ormeci, W. Carrillo-Cabrera, U. Burkhardt et al.

Citation: J. Appl. Phys. **110**, 043715 (2011); doi: 10.1063/1.3625233
View online: http://dx.doi.org/10.1063/1.3625233
View Table of Contents: http://jap.aip.org/resource/1/JAPIAU/v110/i4
Published by the American Institute of Physics.

Transport properties of the clathrate $BaGe_5$

C. Candolfi,[a] U. Aydemir, A. Ormeci, W. Carrillo-Cabrera, U. Burkhardt, M. Baitinger, N. Oeschler, F. Steglich, and Yu. Grin[b]
Max-Planck-Institut für Chemische Physik fester Stoffe, Nöthnitzer Str. 40, 01187 Dresden, Germany

(Received 20 May 2011; accepted 13 July 2011; published online 25 August 2011)

We report on the synthesis, crystallographic and transport properties of the Zintl phase $BaGe_5$, which crystallizes in a new clathrate-type structure. This compound was synthesized by the decomposition of the type-I clathrate $Ba_8Ge_{43}\square_3$ subjected to annealing treatment at 623, 673 and 793 K. Electrical resistivity, thermopower and thermal conductivity measurements were performed in the temperature range 2 – 773 K and complemented by magnetization, specific heat and Hall experiments below room temperature. Additional information on the chemical bonding and electronic band structure in $BaGe_5$ was obtained through the electron localizability indicator (ELI) and the total density of states, all calculated within the all-electron full-potential local orbital method (FLPO). In agreement with the chemical bonding and electronic band structure calculations, electrical resistivity and specific heat data show that $BaGe_5$ is a semiconductor. The complex crystal structure of $BaGe_5$ contributes to the low thermal conductivity which displays a conventional crystalline-like behavior. Further measurements were carried out on samples annealed at 623, 673 and 793 K for four up to 30 days to probe possible variations of the crystal structure and electronic properties as a function of the annealing temperature and time. Even though the annealing temperature does not alter the semiconducting nature of this material, differences in the absolute values of the transport properties were unveiled in samples annealed for short-time periods. These differences are significantly reduced in samples which underwent long-time annealing treatment even though the measured curves do not merge completely. © *2011 American Institute of Physics*. [doi:10.1063/1.3625233]

I. INTRODUCTION

Various intermetallic clathrates have been synthesized over the last decades paving the way to the study of intriguing electronic properties in covalently-bonded frameworks such as superconductivity, glass-like thermal transport or high thermoelectric efficiency.[1–3] The crystal structure of clathrates is composed by a three-dimensional arrangement of polyhedral cages formed by mainly group 14 elements in which cations such as alkaline or alkaline-earth atoms can be encapsulated. Several intermetallic clathrate types have been discovered so far such as the so-called type-I, type-II or chiral clathrates.[4] The cage-like crystal structure of these compounds coupled with the possibility to finely tune the carrier concentration via partial substitutions makes them prospective candidates for thermoelectric applications. These requirements are quantitatively captured through the dimensionless thermoelectric figure of merit $ZT = \alpha^2 T/\rho\lambda$ where α is the thermopower, ρ is the electrical resistivity, λ is the total thermal conductivity and T is the absolute temperature.[5]

Recently, $BaGe_5$ has been identified as a new clathrate type crystallizing in the orthorhombic space group *Pmna* (Pearson symbol *oP*60) (Ref. 6). At the border of covalently-bonded frameworks, the orthorhombic structure comprises dodecahedral cages and infinite channels reminiscent to those of the type-I ($Ba_8Ge_{43}\square_3$) and chiral *cP*124 (Ba_6Ge_{25}) clathrates, respectively. $BaGe_5$ is stable only up to 793 K and decomposes upon heating into Ba_6Ge_{25} and α-Ge (Ref. 6). Since the reverse reaction is kinetically hindered and conventional solid state synthesis techniques do not enable a direct synthesis, this phase remained undetected for a long time. Further, the lack of phase-pure samples of $Ba_8Ge_{43}\square_3$ made it impossible to produce $BaGe_5$ at high yield, an essential requirement to reliably investigate its crystal structure and electronic properties. This difficulty could be recently overcome using a quenching technique with steel plates.[7,8] A further annealing treatment of phase-pure type-I clathrate $Ba_8Ge_{43}\square_3$ in the 573 – 793 K temperature range then resulted in the formation of $BaGe_5$ with a small amount of α-Ge (Ref. 6). With the charge balance $Ba^{2+}[(3b)\text{-}Ge^{-}]_2[(4b)Ge^0]_3$, $BaGe_5$ can be classified as an electron-precise Zintl phase which is in agreement with preliminary measurements including electrical resistivity and magnetic susceptibility.[6] The complex crystal structure together with the semiconducting nature of this compound may therefore lead to promising thermoelectric properties. In this regard, since $BaGe_5$ may be the parent compound of a new class of thermoelectric materials, a detailed investigation of its transport properties may serve as a useful reference for future studies on possible ternary and quaternary derivatives.

In this paper, we report a thorough theoretical and experimental investigation on the relation between crystal structure and transport properties of $BaGe_5$. Synchrotron X-ray powder diffraction was performed on samples annealed at 673 and 773 K to probe possible variations of the crystal structure with the annealing temperature. Transport

[a]Electronic mail: candolfi@cpfs.mpg.de.
[b]Electronic mail: grin@cpfs.mpg.de.

properties measurements including electrical resistivity, thermopower, Hall effect, thermal conductivity and specific heat were performed in a wide temperature range to properly assess the thermoelectric potential of this material. Additional information on the electronic band structure was obtained through first-principles density functional theory calculations.

The paper is organized in the following way. After the description of the experimental and computational methods used (Sec. II), the results are presented and discussed in Section III under seven sub-sections. In the first sub-section (Sec. III A), a detailed description of the crystal structure and the chemical characterizations are given followed by the presentation of the electronic band structure calculations (Sec. III B). The third sub-section (Sec. III C) presents a discussion on the effects of the annealing temperature and time on the transport properties. Magnetic susceptibility and Hall data which may provide additional hints suggesting that subtle variations in the crystal structure arise from differing annealing conditions are shown in Secs. III D and E, respectively. Finally, the last two sub-sections (Secs. III F and G) show the transport properties of a sample annealed at 673 K for 30 days, the samples annealed at 623 and 793 K exhibiting similar electronic properties. The conclusions are collected in Sec. IV.

II. EXPERIMENTAL AND COMPUTATIONAL DETAILS

A. Synthesis

So far, $BaGe_5$ could be only obtained via decomposition of the high-temperature phase $Ba_8Ge_{43}\square_3$ at temperatures below 793 K (Ref. 6). The synthesis of pure $Ba_8Ge_{43}\square_3$ from the elements (Ba pieces, Chempur, 99.9%; Ge pieces, Chempur, 99.9999%) by quenching of the melt was recently described in detail.[7,8] Samples investigated in this work were prepared as follows: Bulk pieces of $Ba_8Ge_{43}\square_3$ were placed in glassy carbon crucibles and sealed in Ta ampoules which were in turn jacketed in argon-filled quartz ampoules. After annealing at constant temperatures varying from 623 K to 793 K for 4 d up to 40 d, the ampoules were quenched in water. In agreement with the starting composition, $BaGe_5$ was obtained in high yield together with $\sim$5 wt-% of α-Ge. No other impurities were detected. Preparation of the samples was carried out under inert atmosphere of an argon-filled dry glovebox. The reaction product was observed to be stable under ambient conditions.

B. Structural and chemical characterizations

All the samples were analyzed by powder X-ray diffraction (PXRD, Huber G670 camera, Guinier geometry, Cu $K\alpha_1$ radiation, $\lambda = 1.540598$ Å, graphite monochromator, $5° \leq 2\theta \leq 100°$, and $\Delta 2\theta = 0.005°$). The reflection positions were determined by profile deconvolution of the powder pattern and corrected using LaB_6 as internal standard [$a = 4.15683(9)$ Å at 295(2) K, Ref. [9]]. The lattice parameters were calculated from the reflection positions by least-squares refinement.

Room temperature synchrotron X-ray data were collected on two samples annealed at 673 K and 793 K (high resolution beamline ID31, ESRF, Grenoble). The measurements were performed in Debye-Scherrer geometry ($\lambda = 0.35415$ Å, $0° \leq 2\theta \leq 40°$, $\Delta 2\theta = 0.001°$) with a multianalyzer stage composed of nine detectors each preceded by a Si (111) crystal. To obtain homogenous powders, the samples were ground with a pestle on an agate mortar, sieved to particle size less than 32 μm and subsequently filled in quartz capillaries ($Ø = 0.5$ mm). All crystallographic calculations were performed using the program package WinCSD (Ref. 9).

To investigate the microstructure of samples, the bulk pieces of the reaction products were polished by using discs of micrometer-sized diamond powders (6, 3, 0.25 μm) and paraffin as lubricant. Polished samples were characterized by a light optical microscope (Zeiss, Axioplan 2) and a scanning electron microscope (Philips XL30, LaB_6 cathode).

Energy dispersive X-ray spectroscopy (EDAX Phoenix system, Si(Li)-detector) was used to identify minority phases and to record overview spectra for the clathrate phase. The precise composition of the clathrate phase was determined by using a wavelength dispersive X-ray spectrometer (WDXS, Cameca SX 100, W cathode) at ten randomly-distributed spots using $Ba_8Ge_{43}\square_3$ as a reference.[7,8]

C. Electronic band structure calculations

An all-electron full-potential scheme employing atom-centered local orbitals (FPLO) was used to investigate the electronic structure and chemical bonding in $BaGe_5$ (Ref. 10). All calculations were carried out within the local density approximation (LDA) to the density functional theory and the exchange-correlation potential was treated with the Perdew-Wang parameterization.[11] The basis sets consisted of Ba: 5*s*, 5*p*/6*s*, 6*p*, 5*d*; Ge: 3*p*, 3*d*/4*s*, 4*p*, 4*d* corresponding to semicore/valence states, respectively. The lower-lying states were treated in a fully-relativistic way, while a scalar-relativistic treatment was applied to the basis sets.

Chemical bonding analysis was performed by applying the electron localizability indicator (ELI) in combination with the electron density (ED).[12] Both quantities in this ELI/ED approach were calculated using the FPLO method and their topological analyses were conducted with the program Basin.[13,14]

D. Transport property measurements

For transport property investigations, samples were annealed at 623, 673 and 793 K for different annealing time periods. Electrical resistivity, thermopower and thermal conductivity were simultaneously measured using the thermal transport option of a Physical Property Measurement System (PPMS-Quantum Design) over the 5 – 350 K temperature range. Contacts onto the samples, cut from the annealed samples with a diamond wire saw to typical dimensions of $2\times2\times10$ mm^3, were realized using four short copper bars attached at 150 °C with a tiny amount of conductive glue (Polytech, EpoTek H20E). Hall measurements were carried out on a PPMS in the 10 – 300 K temperature range and under applied magnetic fields of up to 5 T. Specific heat measurements were realized from 300 K down to 1.9 K on a PPMS using a relaxation method. Magnetic susceptibility was measured under an external magnetic field of 1 T over

the 2 – 300 K temperature range using a MPMS SQUID magnetometer (Quantum Design).

The electrical resistivity and thermopower were measured in the temperature range 300 – 773 K using a commercial setup (ZEM-3, Ulvac-Riko). High temperature thermal conductivity was determined up to 773 K by measuring the thermal diffusivity a using a Netzsch LFA 457 apparatus. The thermal conductivity was then calculated via $\lambda = aC_p\rho_v$ where C_p is the specific heat and ρ_v is the density of the samples. For this experiment, a prism-shaped sample (1 mm thick and 6×6 mm^2) was cut with a diamond wire saw. Specific heat measurements were performed in the 200 – 773 K temperature range on a Netzsch Pegasus differential scanning calorimetry (DSC). No corrections for thermal dilatation were applied. For the thermopower and electrical resistivity, a good agreement between the low and high temperature data sets was observed at 300 K, the deviation never exceeding 8%. Because of the contribution of radiations which are inherent to the method used at low temperatures, a slightly higher discrepancy was observed in the thermal conductivity data ($\sim$ 15%).

III. RESULTS AND DISCUSSION

A. Structural and chemical characterizations

1. Crystal structure

The crystal structure of $BaGe_5$ contains characteristic layers of dodecahedra Ge_{20}, which are condensed via common pentagons and hexagons (Fig. 1(a)] (Ref. 6). The layers are linked by covalent bonds of (3b)Ge^- anions, which alternatively occupy closely adjacent split positions [Fig. 1(b)]. The Ba1 atoms are located in the Ge_{20} dodecahedral cages while the Ba2 and Ba3 atoms are located in open cages resembling the Ge_{24} cages, which are fundamental building blocks e.g., in the type-I clathrate.[4] As Ba2 and Ba3 are arranged in between the layers, their local environment depends strongly on the actual position of the (3b)Ge^- anions Ge4 and Ge5 (Fig. 2).

In space group *Pmna*, the alternatively occupied split positions are statistically arranged with the boundary condition that only reasonable distances of d(Ge-Ge) $\approx$ 2.5 Å in the local environments of the Ge^- anions occur. From PXRD and selected area electron diffraction (SAED) measurements at room temperature, we did not find any hint for an ordering of the half-occupied Ge4 and Ge5 positions. However, partial ordering of the split positions in an isomorphic subgroup cannot be fully ruled out by PXRD. A static atomic ordering may be achieved depending on annealing conditions or a dynamic ordering as a function of temperature. Ordered connection patterns might be realized e.g., in direct subgroups *Pma*2 or *Pmn*2_1 (Fig. 3). To check for any variation of the crystal structure as a function of the annealing temperature, synchrotron X-ray powder data were collected and compared for samples annealed for 10 d at 673 K and 793 K. The Rietveld refinements of both data sets revealed no resolvable variations in the structural parameters (Table I). To check for dynamic atomic rearrangements, *in situ* diffraction experiments will be required.

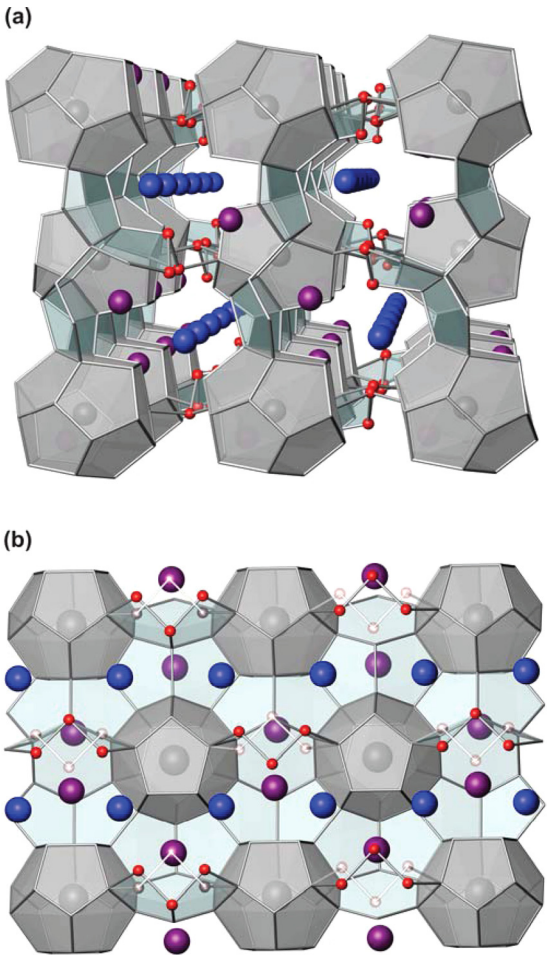

FIG. 1. (Color online) (a) Crystal structure of $BaGe_5$ along [100]. (b) Covalently bonded Ge layer in a view along [010]. Ba1 atoms (gray) are located inside Ge_{20} dodecahedral cages, the Ba2 atoms (blue) are assembled in channels and Ba3 atoms (purple) are found in open Ge_{24} cages. Alternative connection patterns of Ge4 and Ge5 atoms are shown in red and white.

$BaGe_5$ constitutes a new structure type which can be considered as intermediate between the *cP*124 clathrate Ba_6Ge_{25} and the clathrate-I $Ba_8Ge_{43}\square_3$: the infinite channels are reminiscent of those of Ba_6Ge_{25}, while the arrangement of pentagons and hexagons resembles the polyhedral cages

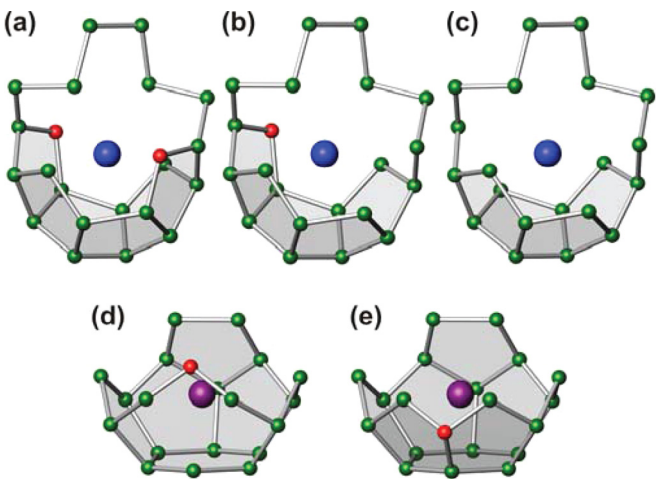

FIG. 2. (Color online) The local environment of Ba2 (a)–(c) and Ba3 (d)–(e) atoms depending on the actual position of Ge4 and Ge5 atoms.

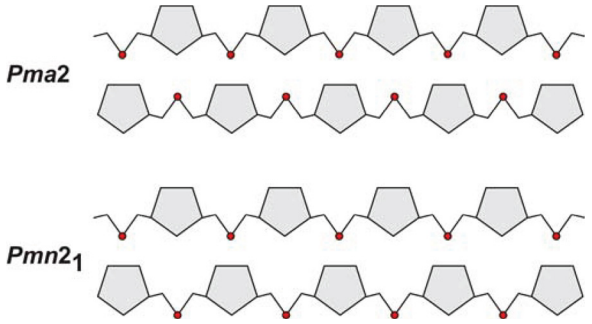

FIG. 3. (Color online) Ordered connection patterns of (3b)Ge^{-} anions Ge4 and Ge5 in the direct subgroups of the space group *Pmna*: *Pma*2 and $Pmn2_1$.

in the clathrate-I $Ba_8Ge_{43}\square_3$. The 2D infinite layers of $BaGe_5$ perpendicular to [010] resemble those of the $A_3Na_{10}Sn_{23}$ type (A = Cs, Rb, K). In $BaGe_5$, the layers are interconnected via the covalent bonds, whereas in $A_3Na_{10}Sn_{23}$ they are fully separated by cations and cluster anions Sn_4^{4-} (Ref. 15).

2. Metallographic analysis

$BaGe_5$ samples obtained from different preparation conditions show no significant differences in the compositions and lattice parameters (Table II). Within the experimental accuracy, a homogeneity range of $BaGe_5$ could not be detected.

The reaction kinetics regarding the transformation of $Ba_8Ge_{43}\square_3$ into $BaGe_5$ and α-Ge depends strongly on temperature. At 793 K, the transformation was already complete after 1 h while at 623 K this was achieved after 40 d. Optical microscopy and scanning electron microscopy (SEM) demonstrate the effect of heat treatment on the microstructure (Fig. 4). The formation of $BaGe_5$ is accompanied by the precipitation of α-Ge at the grain boundaries and, to a smaller extent, as finely dispersed particles with point or needle-like morphology inside the $BaGe_5$ grains (Fig. 4). The coexistence of α-Ge and $BaGe_5$ is consistent with the composition $Ba_{15.7}Ge_{84.3}$ of the starting material Ba_8Ge_{43}, as both clathrates differ by ≈ 1 at % Ge. Due to their small dimensions, the composition of the dispersed particles could not be analyzed with high accuracy, but their dark shade in BSE images agrees well with that of α-Ge at the grain boundaries. Annealing at higher temperatures leads to a rounding of the dispersed α-Ge needles and an almost spherical morphology of these particles was observed after 30 d at 793 K (Fig. 4). Annealing for longer periods (30 d or 40 d) results in elongation of the $BaGe_5$ grains reaching up to 500 μm.

TABLE I. Crystallographic data for $BaGe_5$.

Formula; molar mass/g mol^{-1}	$BaGe_5$; 500.37	
Preparation temperature/K	673	793
Crystal system; space group	Orthorhombic; *Pmna* (no. 52)	
a, *b*, *c*/Å	10.7265(8), 9.2839(5), 14.791(1)	10.7246(9), 9.2860(8), 14.797(1)
Unit cell volume/Å^3	1472.9(3)	1474.1(4)
Z; Density ρcalc/g cm^{-3}	10; 5.640(1)	10; 5.635(2)
Diffractometer	Nine-crystal multi-analyzer stage	
Wavelength λ/Å; monochromator	0.35415; Si 111 crystal	
T/K	RT	
θ range/°	0 to 11.3	
Absorption coefficient μ/mm^{-1}	16.60	
F(000)/e	2160	
Reflections in measured range	1064	
Refined parameters	38	
Refinement method	Rietveld	
R_i; R_p; R_{wp}	0.066; 0.107; 0.086	0.063; 0.113; 0.090

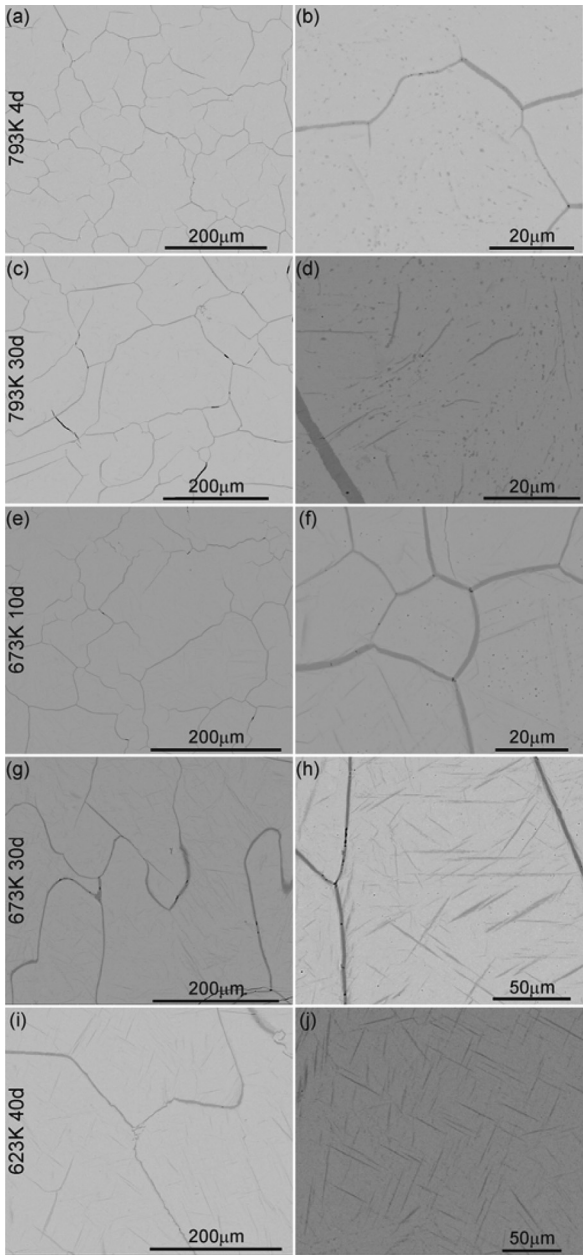

FIG. 4. SEM images (back-scattered electron contrast) of samples obtained via decomposition of $Ba_8Ge_{43}\square_3$ at 793 K in 4d [(a) and (b)] and 30d [(c) and (d)], at 673 K in 10d [(e) and (f)] and 30d [(g) and (h)] and at 623 K in 40d [(i) and (j)]. The figures show formation of large $BaGe_5$ grains and the precipitation of α-Ge within and at the boundaries of $BaGe_5$ grains. $BaGe_5$ and α-Ge are shown as light and dark gray areas, respectively.

TABLE II. Chemical composition and lattice parameters of $BaGe_5$ after different annealing treatments

Starting composition	Preparation route		a, b, c (Å)	Composition (WDXS)
	Temperature (K)	Time (days)		
$Ba_{15.69}Ge_{84.31}$ (Ba_8Ge_{43})	793	4	10.7224(7), 9.2841(7), 14.794(1)	$Ba_{1.00(2)}Ge_{5.00(2)}$
		10	10.7246(9), 9.2860(8), 14.797(1)	$Ba_{0.98(1)}Ge_{5.02(1)}$
		30	10.7252(7), 9.2867(6), 14.795(1)	$Ba_{0.99(1)}Ge_{5.01(1)}$
	733	10	10.7255(9), 9.2871(8), 14.797(1)	$Ba_{0.99(1)}Ge_{5.01(1)}$
	673	4	10.7273(7), 9.2855(6), 14.792(1)	$Ba_{0.98(1)}Ge_{5.02(1)}$
		10	10.7265(8), 9.2839(5), 14.791(1)	$Ba_{0.99(1)}Ge_{5.01(1)}$
		30	10.7261(7), 9.2848(7), 14.794(1)	$Ba_{0.99(1)}Ge_{5.01(1)}$
	623	40	10.7267(9), 9.2851(8), 14.798(1)	$Ba_{1.00(1)}Ge_{5.00(1)}$

High resolution transmission electron microscopy (HRTEM) investigations on a sample obtained after long-term annealing for almost three months at 733 K, revealed elongated crystals of $BaGe_5$, which are oriented almost parallel to each other and perpendicular to the [010] direction (Fig. 5). The arrangement of $BaGe_5$ crystals along selected directions suggests a crystallographic relation between $BaGe_5$ and $Ba_8Ge_{43}\square_3$. In addition, planar defects perpendicular to [010] were observed, which are assumed to be antiphase (010) boundaries.[16]

B. Electronic band structure and chemical bonding

As the crystal structure of $BaGe_5$ contains two Ge sites with half occupancy (Ge4 at 4*h* and Ge5 at 8*i*, see Table III) different structure models with fully occupied sites are necessary for electronic structure calculations. Subgroups of the original space group *Pmna* were considered only for the same unit cell dimensions. Three direct subgroups of *Pmna* allow the half-occupied positions to be split into separate positions: $Pmn2_1$ (no. 31), *Pma*2 (no. 28) and *P*2/*m* (no. 10). Space group *P*2/*m* was not further considered, because in this setting, unphysically short Ge5-Ge5 contacts of $d \approx 0.9$ Å occur. In the $Pmn2_1$ and *Pma*2 subgroups, both the 4*h* and 8*i* sites of the original space group *Pmna* are transformed into two sites with half multiplicity. Each subgroup allows two ordered models, one of which results in Ge4-Ge5 contacts of ≈ 2.0 Å which is much shorter than typical Ge-Ge distances. The other choice shows reasonable Ge-Ge distances. In each subgroup, the latter model has a lower total energy than the former by 0.16 eV.atom^{-1}. Furthermore, the former model yields a metallic density of states (DOS), in clear contradiction with the experimental findings. On the other hand, the model with reasonable Ge-Ge distances leads to band gaps of 0.24 eV and 0.22 eV for $Pmn2_1$ and *Pma*2, respectively. These calculations are thus consistent with the semiconducting behavior of this compound.[6] The total energies computed in both subgroups are very close which might explain the absence of a superstructure or failure to refine the crystal structure within an ordered model in various subgroups. Hence, the distribution between alternative positions might depend on the annealing temperature according to $\Delta G = \Delta H - T\Delta S$.

The electronic DOS obtained using the ordered models are shown in Fig. 6. As can be seen, both models lead to very similar electronic structures. The region between −12.3 and −7 eV mainly originates from Ge 4*s* states. The contribution of Ge 4*p* states is comparable to that of 4*s* states in the −7 and −5.3 eV energy range and becomes dominant between −4.2 and 0 eV. Among the Ba states, 5*d* is the most important one. Ba 5*d* occupancies calculated from projected DOS vary between 0.7 and 1.2 electrons depending on the Ba site symmetry. Figure 6(b) compares the averaged Ge4*p* and Ba 5*d* projected DOS as obtained in $Pmn2_1$. Ge atoms are divided into two groups as 3-bonded and 4-bonded. Ba 5*d* contributions are sizable mainly in the energy range −4 and 0 eV, becoming comparable to (4b)Ge 4*p* contributions between −1 and 0 eV. The (3b)Ge atoms have lone pairs which are usually formed by nonbonding states which do not disperse much in **k**-space and give rise to isolated and sharp features in DOS. However, in complex crystal structures with many atoms in the unit cell both bonding and lone pair

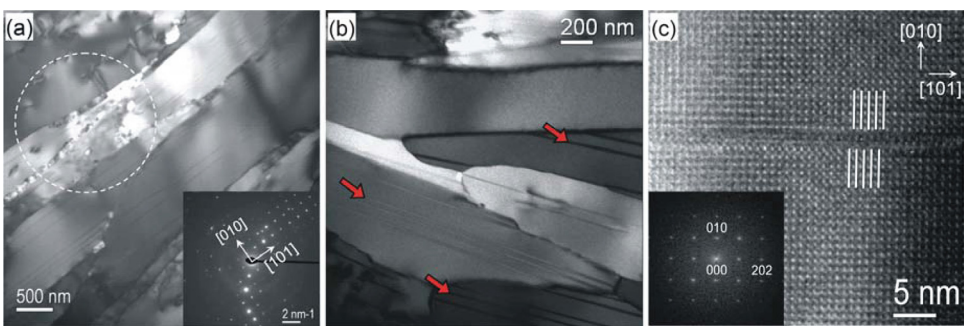

FIG. 5. (Color online) (a),(b) TEM images for a FIB thin cut of a sample, obtained by decomposition of $Ba_8Ge_{43}\square_3$ at 733 K in almost three months, show elongated crystals of $BaGe_5$ with defects quasi-parallel to [101]. (c) HRTEM image taken along [10$\bar{1}$] illustrating a planar defect, a (010) antiphase boundary. In the [10$\bar{1}$] projection, the upper part is shifted by half a period along the [101] direction. The insets in (a) and (c) are SAED pattern of the area marked by circle and the Fast Fourier Transform (FFT) of the lower part of the shifted area, respectively.

TABLE III. Atomic coordinates, displacement parameters (in Å^2) and site occupancies for $BaGe_5$ (top: sample obtained at 673 K, bottom: sample obtained at 793 K).

Atom	Site	*x*	*y*	*z*	*Uiso*	*Occ.*
Ba1	2*a*	0	0	0	0.0120(9)	1.0
Ba2	4*g*	1/4	0.4237(3)	1/4	0.0215(8)	1.0
Ba3	4*h*	0	0.2048(3)	0.6324(2)	0.0374(9)	1.0
Ge1	4*h*	0	0.3641(4)	0.1102(3)	0.008(1)	1.0
Ge2	4*h*	0	0.2136(4)	0.3807(3)	0.006(1)	1.0
Ge3	4*h*	0	0.1451(4)	0.2147(3)	0.008(1)	1.0
Ge4	4*h*	0	0.4668(9)	0.4091(5)	0.010(3)	0.5
Ge5	8*i*	0.3377(4)	0.5073(8)	0.0310(3)	0.005(2)	0.5
Ge6	8*i*	0.3049(3)	0.0939(3)	0.0608(2)	0.0073(8)	1.0
Ge7	8*i*	0.1194(3)	0.7216(3)	0.1550(2)	0.0090(8)	1.0
Ge8	8*i*	0.1807(3)	0.3084(3)	0.0060(2)	0.0074(8)	1.0
Ge9	8*i*	0.3181(3)	0.0205(3)	0.6850(2)	0.0063(8)	1.0
Atom	Site	*x*	*y*	*z*	*Uiso*	*Occ.*
Ba1	2*a*	0	0	0	0.0122(9)	1.0
Ba2	4*g*	1/4	0.4233(3)	1/4	0.0238(8)	1.0
Ba3	4*h*	0	0.2046(3)	0.6317(2)	0.0339(9)	1.0
Ge1	4*h*	0	0.3643(4)	0.1106(3)	0.006(1)	1.0
Ge2	4*h*	0	0.2149(4)	0.3802(3)	0.007(1)	1.0
Ge3	4*h*	0	0.1459(4)	0.2148(3)	0.007(1)	1.0
Ge4	4*h*	0	0.4669(8)	0.4085(5)	0.010(2)	0.5
Ge5	8*i*	0.3365(4)	0.5075(7)	0.0310(3)	0.006(1)	0.5
Ge6	8*i*	0.3058(2)	0.0937(3)	0.0609(2)	0.0070(7)	1.0
Ge7	8*i*	0.1196(3)	0.7219(3)	0.1551(2)	0.0078(7)	1.0
Ge8	8*i*	0.1807(3)	0.3085(3)	0.0056(2)	0.0070(6)	1.0
Ge9	8*i*	0.3183(2)	0.0201(3)	0.6846(2)	0.0062(7)	1.0

The positions of Ge4 and Ge5 are alternatively occupied and were fixed to 0.5 at the final stage of the refinement. Free refinement of the occupancies led to the values 0.510(5) for Ge4 and 0.500(3) for Ge5 for the sample obtained at 673 K and 0.518(5) for Ge4 and 0.499(3) for Ge5 for the sample obtained at 793 K.

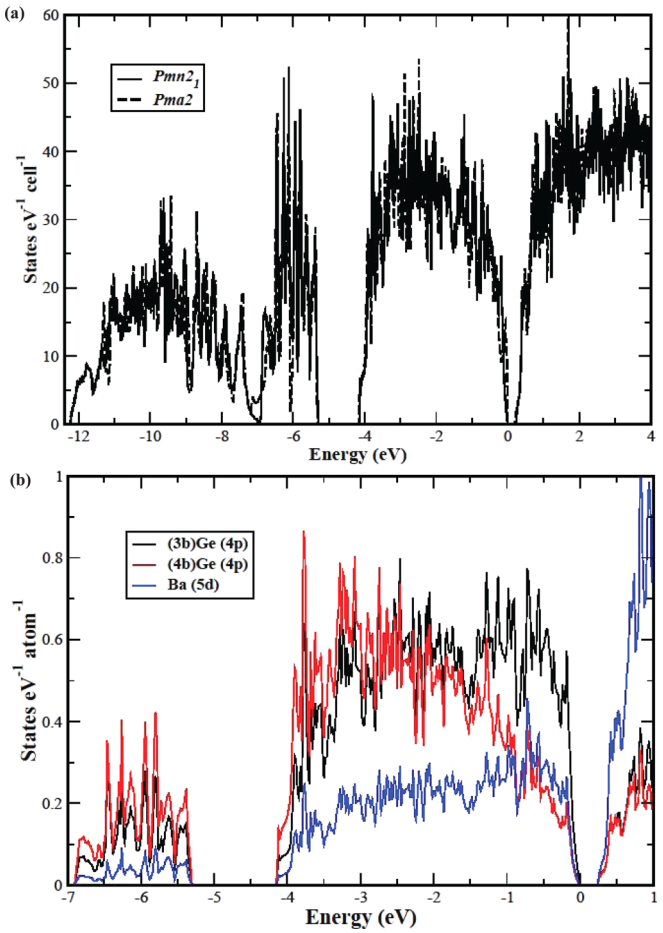

FIG. 6. (Color online) (a) Energy dependence of the total density of states of $BaGe_5$ calculated in the space groups $Pmn2_1$ and *Pma*2. (b) Comparison of projected DOS averaged for (3b)Ge, (4b)Ge and Ba atoms for $Pmn2_1$ case.

related states overlap in energy making a clear identification difficult. Nonetheless, due to the contrast between the DOS of (3b)Ge and (4b)Ge 4*p* between −1 and 0 eV, it is plausible to assume that lone pairs have contributions from the (3b)Ge 4*p* states in this interval.

The unit cell of $BaGe_5$ contains in total 60 atoms ($Z = 10$) with 20 three-bonded and 30 four-bonded Ge atoms. Formally, the charge of 10 Ba^{2+} cations is balanced by 20 (3b)Ge^- anions in accordance with $[Ba^{2+}]_{10}[(3b)Ge^-]_{20}[(4b)Ge^0]_{30}$ (Ref. 6). Thus, $BaGe_5$ can be considered as a semiconducting Zintl phase with a narrow bandgap in agreement with the band structure calculations. Chemical bonding analysis based on the ELI concept further corroborates this expectation. The ELI attractors in the valence region are found to be of dysnaptic and monosynaptic type. The former corresponds to two-centered Ge-Ge bonds with an electron population of ≈ 2 while the latter is related to lone-pair-like features (Fig. 7). The computed electron counts in the Ge-Ge bonds vary between 1.7 (bond length: 2.58 Å) and 2.2 (bond length: 2.45 Å). Electron population in the lone-pair basins of the three-bonded Ge atoms at fully occupied sites is close to 2.3 while it is 2.4 and 2.2 for Ge4 and Ge5, respectively. It is expected that the diamagnetic increment of a Ge atom with a lone pair differs from that of a Ge atom in α-Ge. Since in $BaGe_5$ 40% of the Ge atoms have lone pairs, estimate of diamagnetic susceptibility based on the tabulated value for α-Ge may be smaller in absolute value than the measured one.

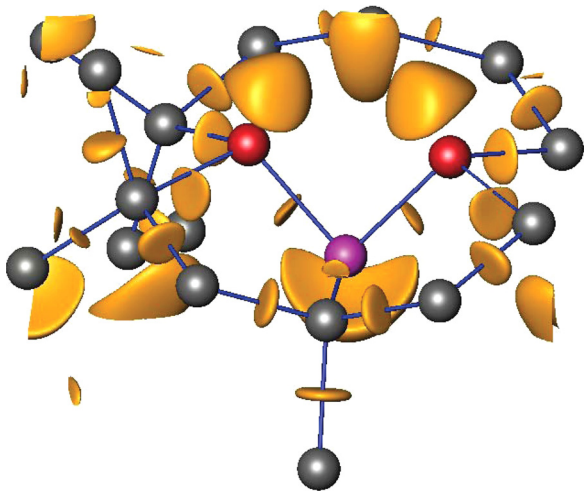

FIG. 7. (Color online) ELI isosurface with $\Upsilon = 1.256$ depicted in the vicinity of the Ge4 and Ge5 sites. The purple and red spheres denote the three-bonded Ge4 and Ge5 atoms, respectively, while the gray spheres represent the Ge atoms at the fully-occupied sites. The lone pairs of Ge4 and Ge5 are clearly visible.

C. Annealing temperature and time effects on the transport properties

Figure 8 depicts the temperature dependence of the electrical resistivity (a), thermopower (b), and thermal conductivity (c) of samples annealed at 623, 673 and 793 K for 40, 10 and 4 days, respectively. As can be seen, differences in the annealing temperature and time do not affect the physical behavior but result in variations in the absolute values of the transport properties. The thermopower decreases in absolute value with increasing annealing temperature to reach −150 to −180 $\mu V.K^{-1}$ at 300 K. While the thermal conductivity values remain similar independent of the annealing temperature, the electrical resistivity is more influenced, the values exhibiting a steeper rise toward low temperatures as the annealing temperature is decreased. Synchrotron X-ray diffraction measurements together with WDXS analyses could not reveal variations in the crystal structure as a function of the synthesis conditions within the experimental accuracy. Thus, the slight variations observed may hint toward an influence of the microstructure. Several aspects revealed by our investigations and discussed in Sec. III A may stand for underlying mechanisms of the observed sensitivity to the synthesis conditions. A first essential result is related to the grain size of the samples, a longer annealing time resulting in larger grains. In addition, the TEM investigations have revealed the presence of planar defects (see Fig. 5) within the $BaGe_5$ grains irrespective of the annealing time. Both microstructural properties, along with the presence of Ge within the $BaGe_5$ grains and at the grain boundaries, likely influence the electrical transport. The strong disorder inherent to the microstructure of the samples may also explain the quasi-insensitivity of the thermal conductivity with respect to the synthesis conditions.

To further shed light on these issues, samples were annealed at the three above-mentioned temperatures during longer periods of 40 and 30 days for the last two samples (Fig. 9). This long-time-annealing treatment results in similar microstructure reflected by similar absolute values and temperature dependences of the transport properties in the whole temperature range. The slightly different electrical resistivity values distinguishable between the samples annealed at 623 or 673 K and 793 K may still originate from small differences in the microstructure of these compounds. The thermopower values, however, do not merge into a single curve suggesting that some differences survive in the samples even after a long-time annealing treatment. Considering that the role played by the microstructure on the thermopower should be of minor importance in the present case, this might indicate the existence of small variations in the crystal structure. Taken as a whole, these results show that the annealing time is the key parameter leading to variations in the microstructure which directly influence the absolute values of the electrical resistivity and thermal conductivity and possibly of the thermopower.

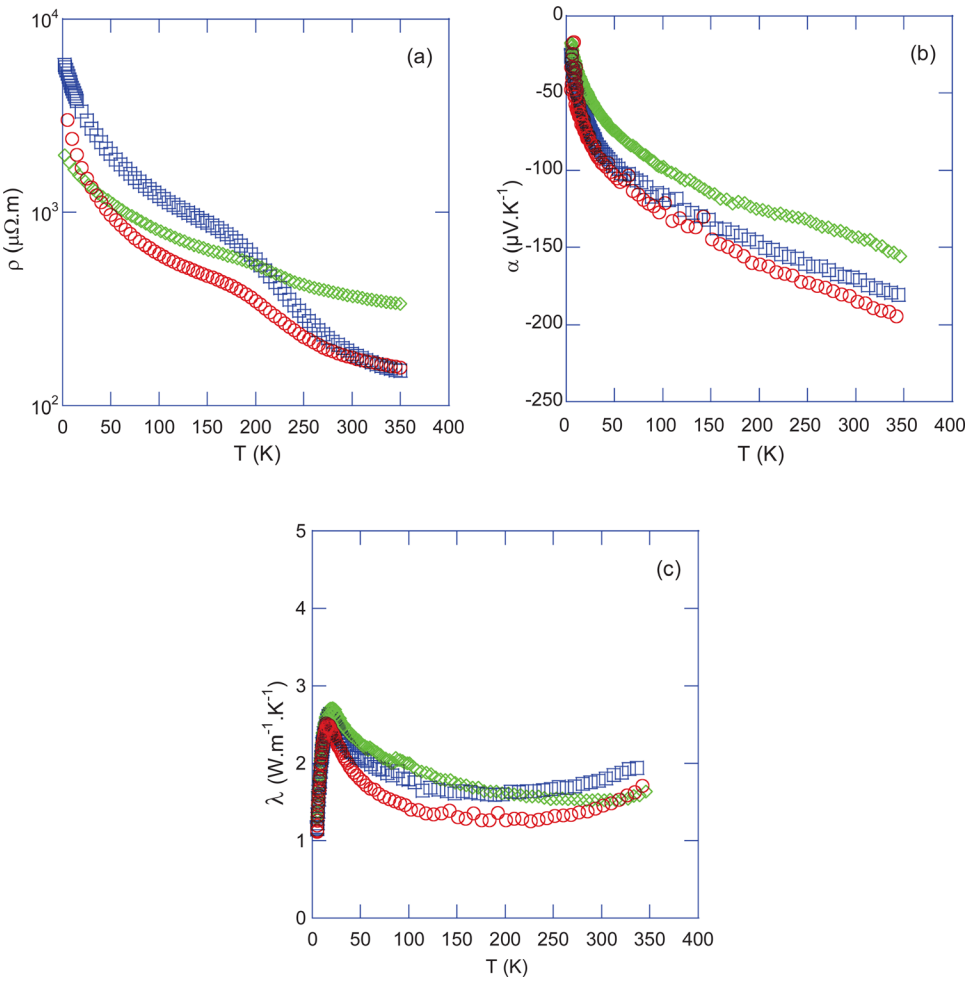

FIG. 8. (Color online) Temperature dependence of the electrical resistivity (a), thermopower (b) and total thermal conductivity (c) of samples annealed at 623 (○), 673 (□) and 793 K (◊) for 40, 10 and four days, respectively.

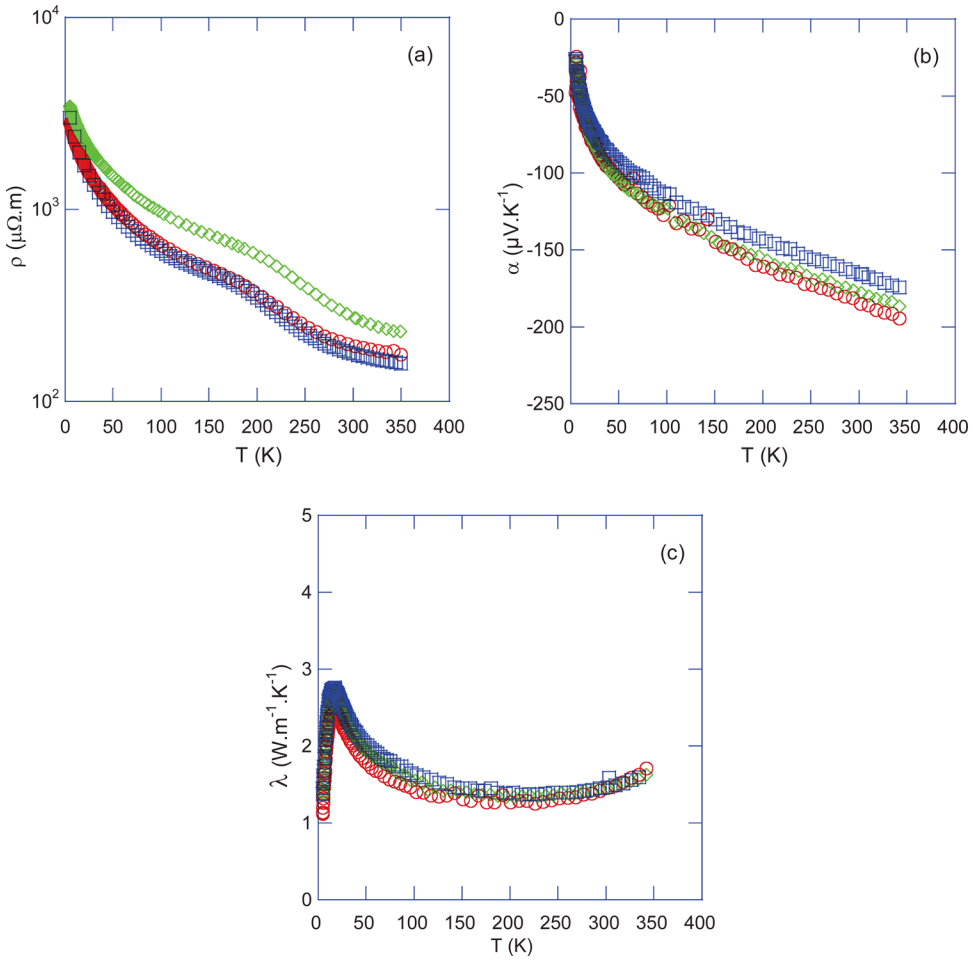

FIG. 9. (Color online) Temperature dependence of the electrical resistivity (a), thermopower (b) and total thermal conductivity (c) of samples annealed at 623 (○), 673 (□) and 793 K (◊) for 40, 30 and 30 days, respectively.

D. Magnetic susceptibility

The temperature dependence of the magnetic susceptibility, χ, is shown in Fig. 10. As reported in our previous study, a $BaGe_5$ sample annealed for ten days at 673 K showed a nearly temperature independent diamagnetism with a slight upturn toward low temperatures probably due to traces of paramagnetic impurities.[6] An estimation of the core diamagnetic contribution, χ_{dia}, using tabulated diamagnetic increments of Ba and Ge (-32×10^{-6} emu.mol^{-1} and -15.7×10^{-6} emu.mol^{-1}, respectively) yielded -110.5×10^{-6} emu.mol^{-1} which is considerably lower in absolute value than the experimental value -210×10^{-6} emu.mol^{-1} at 300 K (Refs. 17 and 18). Interestingly, the magnetic susceptibility of samples annealed for a longer period (30–40 days) exhibits significantly smaller absolute values. At room temperature, $\chi(T)$ amounts to -135×10^{-6} emu.mol^{-1} which appears in good agreement with the calculated value. These results thus show that the magnetic properties of all samples develop similarly with annealing time reflecting intrinsic properties. Further, chemical characterizations have not only shown similar compositions regardless of the annealing temperature within our experimental accuracy but have also indicated the presence of elemental Ge as the only secondary phase. It seems therefore unlikely that such large variations originate from small differences in the microstructure of these samples. An alternative explanation might therefore be related to the increments of Ba^{2+} and α-Ge used for the above-mentioned estimate,[17,18] the difference arising from the high content of Ge^{-} anions in $BaGe_5$ which may lead to variations in the diamagnetic contributions of the Ge atoms with the annealing time. Our crystallographic investigations have revealed an inherent disorder on the Ge4 and Ge5

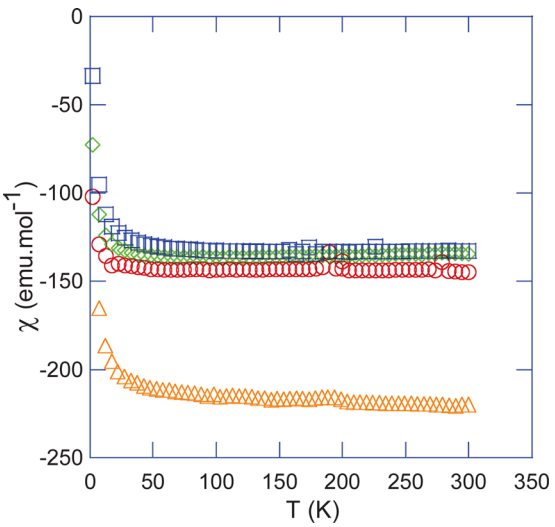

FIG. 10. (Color online) Temperature dependence of the magnetic susceptibility of the samples annealed at 623 (○), 673 (□) and 793 K (◊) for 40, 30 and 30 days, respectively. For comparison purposes, data collected on a sample annealed at 673 K (Δ) for ten days (Ref. 6) have been added.

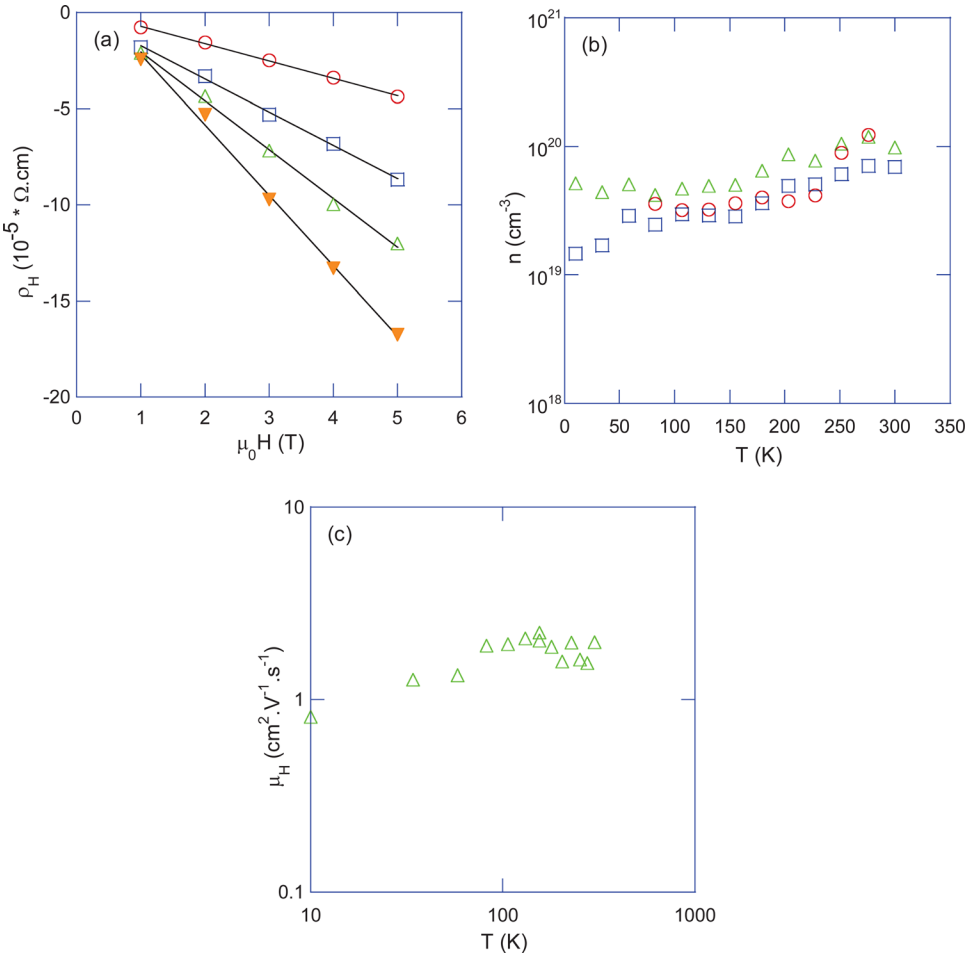

FIG. 11. (Color online) (a) Hall resistivity, ρ_H, as a function of the magnetic field at 300 (○), 180 (□), 82.5 (Δ) and 35 K (▼) of the illustrative sample annealed at 673 K for 30 days. (b) Temperature dependence of the carrier concentration inferred from the Hall effect data for the samples annealed at 623 (○), 673 (□) and 793 K (Δ) for 40, 30 and 30 days, respectively. (c) Temperature dependence of the Hall mobility, μ_H, of the illustrative sample annealed at 793 K for 30 days.

sites preventing a superstructure to be observed. As discussed above, Ge atoms at these sites have lone pairs. As atoms with lone pairs have in general a strong influence on the diamagnetic behavior, the actual arrangement of these atoms in the crystal structure might be a reason for the different $\chi(T)$ values observed after annealing. The fact that a longer annealing time leads to a closer agreement between the experimental and theoretical values may be interpreted as a lower amount of defects in the crystal structure with annealing time. In this regard, whether longer annealing times may result in a fully ordered crystal structure remains an interesting and open question which warrants further investigations.

E. Hall effect

The magnetic field dependence of the Hall resistivity, $\rho_H(\mu_0 H)$, shown for selected temperatures, of the sample annealed at 673 K for 30 days is depicted in Fig. 11(a). To dismiss any magnetoresistive contribution and thus, to reliably extract the charge carrier concentration, the antisymmetric part of the transverse resistivity under magnetic field reversal was determined via $[\rho_H(+\mu_0 H) - \rho_H(-\mu_0 H)]/2$. Regardless of the annealing temperature, this results in linear variations of the $\rho_H(\mu_0 H)$ curves characterized by a negative slope in the whole temperature range indicating a dominant electron-like response. Within a single-band model, the electron concentration, n, can then be derived from the Hall coefficient, $R_H = \rho_H/\mu_0 H$, following the relation $n = 1/R_H e$ where e is the elementary charge. As shown in Fig. 11(b), n shows similar temperature dependence for all samples indicative of an activated behavior, consistent with the semiconducting nature of $BaGe_5$. However, varying the annealing temperature leads to slight variations in n which ranges between 7.1×10^{19} and 1.2×10^{20} cm^{-3} at 275 K. These variations are consistent with the slight differences observed in the thermopower data [see Fig. 9(b)] and point to subtle changes of the crystal structure depending on the annealing temperature. Hall measurements therefore provide further evidence showing possible variations in the crystal structure as a function of the annealing temperature. The Hall mobility of the charge carriers, μ_H, derived via the relation $\mu_H = R_H/\rho$, is low for all samples and in the order of a few $cm^2.V^{-1}.s^{-1}$ in the whole temperature range. Further, μ_H, shown in Fig. 11(c) for the illustrative sample annealed at 793 K for 30 days, shows a very slight increase below ~ 100 K before exhibiting constant values up to 300 K indicative of neutral impurities as the main source of diffusion of the charge carriers ($\mu_H \sim$ cst).

F. Specific heat

Figure 12(a) shows the temperature dependence of the specific heat, C_p, of the sample annealed at 673 K for 30

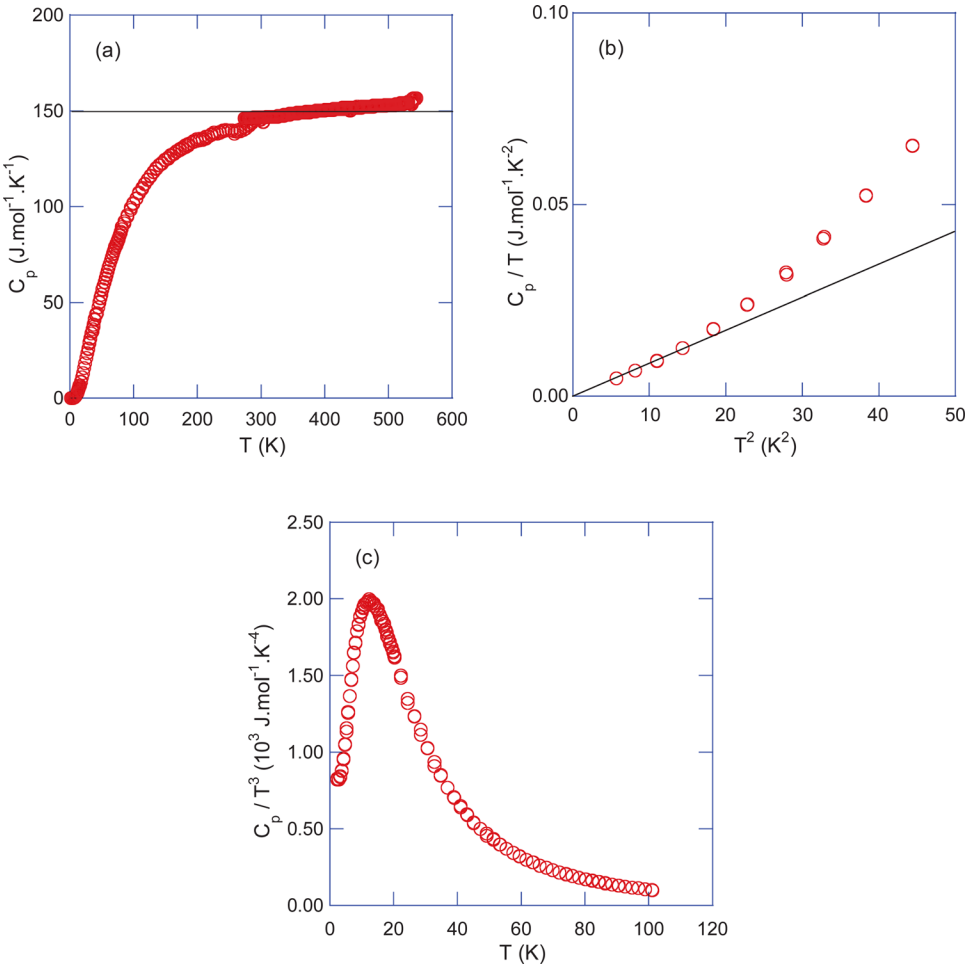

FIG. 12. (Color online) (a) Specific heat, C_p, as a function of the temperature. The horizontal solid line stands for the Dulong-Petit value. (b) C_p/T as a function of T^2. The solid line is a guide to the eye to underline the narrow temperature window where a linear dependence is observed. (c) C_p/T^3 as a function of T to highlight the low temperature peak possibly related to thermal motion of Ba2 and Ba3 atoms.

days in the 1.9 – 550 K temperature range. Note that varying the annealing temperature does not lead to variations in $C_p(T)$ within the experimental accuracy. Above room temperature, the $C_p(T)$ values increase with increasing temperature reflecting the anharmonicity of the lattice contribution. The observed values, however, are very close to those expected from the Dulong-Petit law predicting a constant value $3NR$, where N is the number of atoms per formula unit. To probe the electronic ground state of these materials, the low temperature data have been plotted as C_p/T versus T^2 [Fig. 12(b)]. A fit of the free-electron formula $C_p/T = \gamma + \beta T^2$ to the data at $T < 4$ K, where γ is the Sommerfeld coefficient of the electronic contribution and βT^2 describes the lattice contribution, yields a γ value indistinguishable from zero within the experimental error and, thus, indicates a semiconducting ground state. The β coefficient is related to the Debye temperature, θ_D, via the relation $\theta_D = [(12\pi^4 NR)/(5\beta)]^{1/3}$ where N is the number of atoms per formula unit and R is the gas constant. Using $\beta = 1.85$ mJ.mol.$^{-1}$.K^{-4} and $N = 6$ as determined from Rietveld refinements, we obtain $\theta_D \approx 233$ K. This value is in accord with the Debye temperature of various Ge-based type-I clathrates and corresponds to that of the parent compound $Ba_8Ge_{43}\square_3$ inferred from specific heat analyses ($\theta_D \approx 232$ K).[7,19] In clathrates, the thermal motion of the entrapped cations leads to an additional contribution to the specific heat that dominates the low temperature variations of $C_p(T)$ and appears as a pronounced peak centered near 15 K. To determine whether or not this contribution is also present in this compound, C_p/T^3 is plotted as a function of T in Fig. 12(c). As can be observed, a peaked structure is resolved near 15 K indicating the presence of low energy optical modes that usually cannot be captured by a single θ_D parameter within the Debye theory. X-ray and neutron diffraction studies carried out on various type-I clathrates have shown that the Ba atoms located in the pentagonal dodecahedra behave as the framework atoms.[4] A similar conclusion can be drawn for $BaGe_5$ as revealed by our Rietveld analyses (see Table III). We can thus safely conclude that these low energy modes are most probably associated to the motions of Ba2 and Ba3 atoms. Even though modeling the dynamics of the Ba atoms in type-I clathrates through Debye and Einstein terms was found to satisfactorily describe the low temperature specific heat, any attempt to apply this model in the present case failed.[7,20–22] This clearly underscores a more complex lattice dynamics in $BaGe_5$ with respect to type-I clathrates. In this regard, it would be of interest to probe these low energy modes with more sensitive techniques such as inelastic neutron scattering or Raman spectroscopy.

G. Thermoelectric properties

Figure 13(a) shows the temperature dependence of the electrical resistivity of the sample annealed at 673 K. The

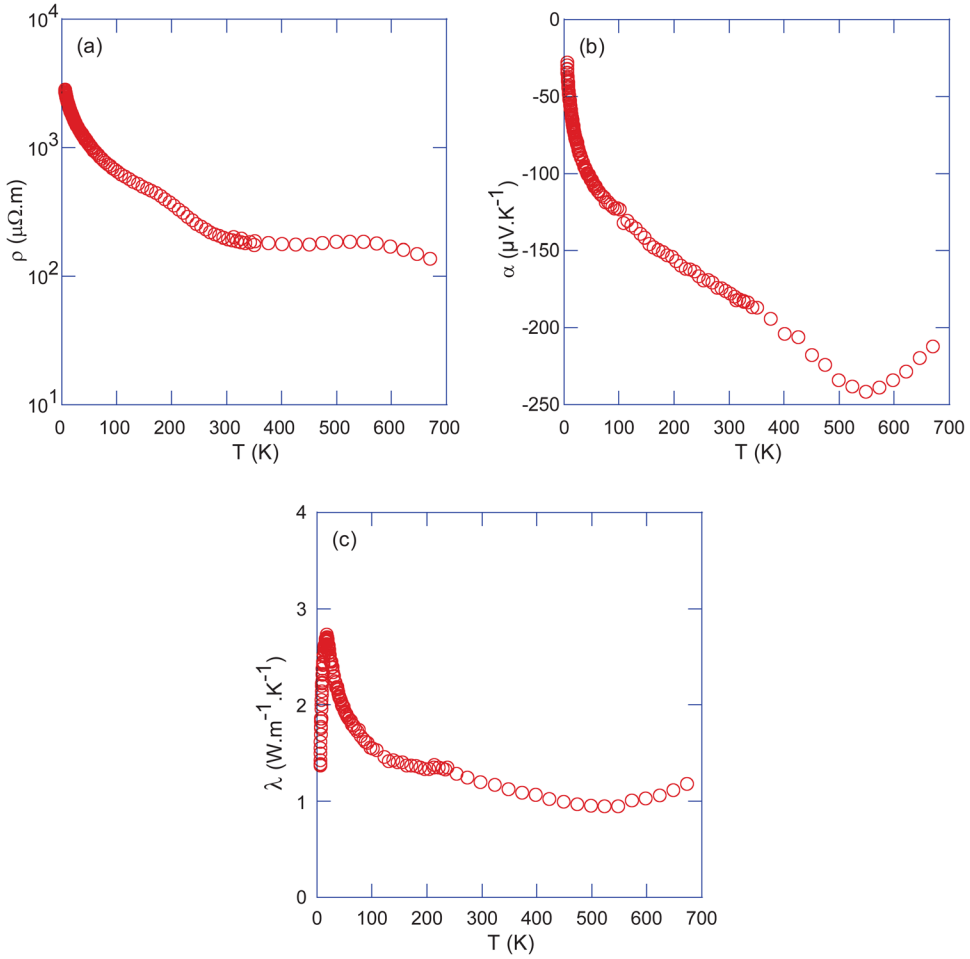

FIG. 13. (Color online) Temperature dependence of the electrical resistivity (a), thermopower (b) and total thermal conductivity (c) of $BaGe_5$.

negative electrical resistivity coefficient $\partial\rho/\partial T$ reflects the semiconducting nature of this material and is thus consistent with the low temperature specific heat data. In addition, an anomaly centered near 180 K can be clearly observed. It is worth mentioning that measurements performed on different samples always led to the presence of this anomaly ruling out an extrinsic origin of this feature. In addition, this anomaly does not lead to a hysteresis effect, the electrical resistivity curves on cooling and warming being strictly similar. Even though this anomaly is not obviously correlated with any features in magnetization, specific heat or transport properties, a possible transition to an ordered crystal structure cannot be strictly ruled out. In this regard, further crystallographic investigations at low temperatures might help discern the origin of this anomaly. A downturn occurring near 550 K characterizes the high temperature behavior of this material and, as shown by the thermopower data, can be attributed to the thermal activation of the minority carriers across the bandgap.

The temperature dependence of the thermopower, depicted in Fig. 13(b), shows that $BaGe_5$ exhibits negative values in the whole temperature range indicative of electrons as the prominent charge carriers in agreement with the Hall data. The low-temperature behavior strongly deviates from a linear behavior expected in degenerate semiconductors and thus, points to a non-degenerate behavior which, together with the high thermopower values measured, is consistent with the semiconducting nature of this compound. Combining the α value and the electron concentration measured at 300 K, the effective mass of electrons m^* can be estimated assuming a single-parabolic band model. Within this description, the thermopower and electron concentration are expressed as

$$\alpha = -\frac{k_B}{e}\left[\frac{(2+\lambda)F_{1+\lambda}(\eta)}{(1+\lambda)F_{\lambda}(\eta)} - \eta\right] \quad (1)$$

$$n = \frac{4}{\sqrt{\pi}}\left[\frac{2\pi m^* k_B T}{h^2}\right]^{\frac{3}{2}} F_{\frac{1}{2}}(\eta) \quad (2)$$

where h is the Planck constant, k_B is the Boltzmann constant, e is the elementary charge, λ is a scattering constant related to the energy dependence of the electronic scattering mechanism and F_i is the Fermi integral of order i defined as

$$F_i(\eta) = \int_0^{\infty} \xi^i f_0(\xi,\eta) d\xi$$

where f_0 is the Fermi distribution function, ξ is the reduced energy of electrons and η is the reduced Fermi level defined as $\eta = E_F/k_BT$. Using $\lambda = 1/2$ for neutral impurity scattering

as suggested by the temperature dependence of the Hall mobility [Fig. 11(c)], this approach leads to an effective mass of $1.4m_0$ (m_0 is the bare electron mass) in line with the values observed in different type-I clathrates.[1]

Above 550 K, $|\alpha|$ decreases with increasing temperature suggesting that this sample experiences minority carrier effect. From the temperature at which this maximum occurs, the bandgap, E_g, can be estimated using the relation $E_g = 2e|\alpha_{max}|T_{max}$ where e is the elementary charge. With $T_{max} = 550$ K and $|\alpha_{max}| = 230\ \mu V.K^{-1}$, we obtain a bandwidth of 236 meV, in good agreement with our band structure calculations.

Figure 13(c) shows the temperature dependence of the total thermal conductivity. $BaGe_5$ exhibits a temperature dependence characteristic of crystalline insulators which feature a dielectric maximum at low temperatures followed by an exponential decrease originating from Umklapp scattering processes. Thus, the higher degree of complexity of the crystal structure of $BaGe_5$ with respect to $Ba_8Ge_{43}\square_3$ does not result in marked differences in the thermal conductivity nor does it lead to glass-like thermal transport as observed in some type-I clathrate compounds.[7,23–25] Because of the semiconducting character of $BaGe_5$ resulting in large electrical resistivity values, the measured λ values almost entirely reflect the lattice contribution, the electronic contribution amounting to $\sim 2.5\%$ at 300 K using the Wiedemann-Franz law $\lambda_e = LT/\rho$ where L is the Lorenz number. Above 550 K, the thermal conductivity increases due to the thermal activation of minority carriers leading to an additional ambipolar contribution in agreement with the electrical resistivity and thermopower data.

The electrical resistivity stands out as the limiting parameter preventing the achievement of very high ZT values in $BaGe_5$. A maximum ZT of ~ 0.2 is reached at 550 K. Further investigations with the aim at tuning the carrier concentration through a partial substitution of Ge may be a worthwhile undertaking to enhance the thermoelectric properties of $BaGe_5$.

IV. CONCLUSION

The transport properties of the new clathrate compound $BaGe_5$ have been investigated in detail under various annealing times and temperatures. A careful analysis of the crystal structure along with the microstructure of the obtained samples revealed no significant differences in the crystal structure within the experimental accuracy. Variations in the microstructure on annealing have direct consequences on the transport properties for which significant differences arise for short-time annealing treatments. These differences are lessened by applying longer annealing times regardless of the applied annealing temperatures. Transport property measurements have indicated a semiconducting nature in agreement with electronic band structure calculations. Even though a low thermal conductivity emerges from the complex crystal structure, the high electrical resistivity values prevent to achieve very high ZT values ($ZT_{max} \sim 0.2$ at 550 K). This might be overcome by ternary variants of $BaGe_5$ thereby optimizing its thermoelectric efficiency. In this regard, our investigations presented herein may serve as a basis for future studies.

ACKNOWLEDGMENTS

I. Margiolaki and Y. Prots are acknowledged for the synchrotron X-ray measurements at ESRF in Grenoble. The authors warmly thank Y. Oztan, Petra Scheppan, Renate Hempel-Weber and members of the Kompetenzgruppe Struktur for providing experimental support. C.C. acknowledges the financial support of the CNRS-MPG program. M.B. and Yu.G. gratefully acknowledge financial support by the Deutsche Forschungsgemeinschaft (SPP 1415, "Kristalline Nichtgleichgewichtsphasen (KNG) - Präparation, Charakterisierung und *in situ*-Untersuchung der Bildungsmechanismen").

[1] M. Christensen, S. Johnsen, and B. B. Iversen, Dalton Trans. **39**, 978 (2010).
[2] E. S. Toberer, M. Christensen, B. B. Iversen, and G. J. Snyder, Phys. Rev. B **77**, 075203 (2008).
[3] S. Yamanaka, Dalton Trans. **39**, 1901 (2010), and references therein.
[4] K. A. Kovnir and A. V. Shevelkov, Russ. Chem. Rev. **73**, 923 (2004).
[5] H. J. Goldsmid in *Thermoelectric Refrigeration* (Temple Press Books Ltd., London, 1964).
[6] U. Aydemir, L. Akselrud, W. Carrillo-Cabrera, C. Candolfi, N. Oeschler, M. Baitinger, F. Steglich, and Yu. Grin, J. Am. Chem. Soc. **132**, 10984 (2010).
[7] U. Aydemir, C. Candolfi, H. Borrmann, M. Baitinger, A. Ormeci, W. Carrillo-Cabrera, C. Chubilleau, B. Lenoir, A. Dauscher, N. Oeschler, F. Steglich, and Yu. Grin, Dalton Trans. **39**, 1078 (2010).
[8] C. Candolfi, U. Aydemir, M. Baitinger, N. Oeschler, F. Steglich, and Yu. Grin, J. Electron Mater. **39**, 2039 (2010).
[9] L. G. Akselrud, P. Y. Zavalii, Yu. Grin, V. K. Pecharsky, B. Baumgartner, and E. Wölfel, Mater. Sci. Forum **335**, 133 (1993).
[10] K. Koepernik and H. Eschrig, Phys. Rev. B **59**, 1743 (1999).
[11] J. P. Perdew and Y. Wang, Phys. Rev. B **45**, 13244 (1992).
[12] M. Kohout, Int. J. Quantum Chem. **97**, 651 (2004).
[13] A. Ormeci, H. Rosner, F. R. Wagner, M. Kohout, and Yu. Grin, J. Phys. Chem. A **110**, 1100 (2006).
[14] M. Kohout, program Basin, version 4.2, Max-Planck-Inst. for Chem. Phys. of Solids, Dresden, Germany, 2008.
[15] S. Bobev and S. C. Sevov, Inorg. Chem. **39**, 5930 (2000).
[16] W. Carrillo-Cabrera, in *Instrumentation and Methodology*, Microscopy Conference MC2009, Graz, Austria, edited by G. Kothleither and M. Leisch (Verlag der TU Graz, Graz, Austria, 2009) Vol. 1, pp. 275–276.
[17] A. Weiss and H. Witte, *Magnetochemie* (Verlag Chemie, Weinheim/Bergstr, 1973), p. 72.
[18] Numerical Data and Functional Relationships in Science and Technology, *Landolt-Börnstein Group III Condensed Matter*, Vol. 41, A1b, edited by O. Madelung, U. Rössler, and M. Schulz (Springer-Verlag, Berlin, 2002).
[19] M. Falmbigl, G. Rogl, P. Rogl, M. Kriegisch, H. Muller, E. Bauer, M. Reinecker, and W. Schranz, J. Appl. Phys. **108**, 043529 (2010).
[20] K. Suekuni, M. A. Avila, K. Umeo, and T. Takabatake, Phys. Rev. B. **75**, 195210 (2007).
[21] M. A. Avila, K. Suekuni, K. Umeo, H. Fukuoka, S. Yamanaka, and T. Takabatake, Phys. Rev. B **74**, 125109 (2006).
[22] N. Melnychenko-Koblyuk, A. Grytsiv, P. Rogl, M. Rotter, E. Bauer, G. Durand, H. Kaldarar, R. Lackner, H. Michor, E. Royanian, M. M. Koza, and G. Giester, Phys. Rev. B **76**, 144118 (2007).
[23] J. L. Cohn, G. S. Nolas, V. Fessatidis, T. H. Metcalf, and G. A. Slack, Phys. Rev. Lett. **82**, 779 (1999).
[24] M. Christensen, N. Lock, J. Overgaard, and B. B. Iversen, J. Am. Chem. Soc. **128**, 15657 (2006).
[25] S. Johnsen, A. Bentien, G. K. H. Madsen, M. Nygren, and B. B. Iversen, Phys. Rev. B **76**, 245126 (2007).